Synthesis, Characterization and Tunable Electronic/ Optical Properties of II−VI Semiconductor Species Included in the Sodalite Structure

Kelly L. Moran,[†] William T. A. Harrison,[‡] Ivo Kamber,[§] Thurman E. Gier, Xianhui Bu, Daniel Herren,[⊥] Peter Behrens,[∥] Hellmut Eckert,* and Galen D. Stucky*

Department of Chemistry, University of California, Santa Barbara, California 93106-9510

Received February 29, 1996[⊗]

The composition-dependent optical and electronic tunability of the sodalite analogues with stoichiometries $Zn_8X_2[BO_2]_{12}$ (X = O, S, Se) and $[Cd_yZn_{(1-y)}]_8X_2[BeSi_xGe_{(1-x)}O_4]_6$ (X = S, Se and Te) have been demonstrated. The materials strongly photoluminesce, and a comparison of the photoluminescence behavior of the single crystals with the as-synthesized powder analogues shows that the visible emission is intrinsic to the sodalite analogue and not due to impurities such as bulk semiconductor. The emission maxima of these materials can be varied by as much as 100 nm with subtle modifications in the host sodalite framework composition and excitation energies can be stored over, at minimum, several minutes. The materials can be prepared either hydrothermally or by high-temperature solid-state reactions. The local and average long-range structures of composition $Zn_8X_2[BO_2]_{12}$ (X = O, S, Se) and $M_8X_2[BeSi_xGe_{1-x}O_4]_6$ (M = Zn, Cd; X = S, Se, Te) are described based on the results of polycrystalline X-ray diffraction, multinuclear solid-state MAS NMR, CdL_3 XANES, UV/visible and photoluminescence spectroscopic measurements. Additionally, the crystal structures of the synthetic helvite solid solutions $Zn_8S_2[BeSi_xGe_{1-x}O_4]_6$ (x = 0.03, 0.37, 0.74) are presented based on refinement of single-crystal X-ray diffraction and selected area electron diffraction data; these materials crystallize in the acentric, cubic space group $P23$ (No. 195) with unit-cell parameters a = 8.250(4), 8.221(2), and 8.163(1) Å, respectively. In all these sodalite analogues, the anionic, rigid sodalite framework encloses $[M_4X]^{6+}$ tetrahedra in a crystalline cubic array, separating each tetrahedron from its eight nearest neighbors by at least 6.4 Å, center to center. This electrostatic isolation results in dramatic high-energy shifts in the optical absorption spectra of the materials and low-frequency shifts in the MAS NMR spectra of the cage center anions, relative to the bulk semiconductors. ^{113}Cd MAS NMR and CdL_3 XANES spectra show that the influence of the anion type on the electronic structure at the Cd^{2+} ions in the cadmium sodalites is small.

Introduction

The optical properties of natural minerals that crystallize with the sodalite structure have fascinated humans since antiquity.[1] More recently the cathodo- and photochromic properties of sodalites have been investigated for potential use in emissive flat panel displays, computer memory and recording, electron lamps, and high-bandwidth/high-efficiency light sources.[2] The composition-dependent coloration and bleaching properties of cathodochromic sodalites have been studied by Tranjan and Todd.[3] Other recent studies of structure-dependent optical properties of sodalites include the characterization of $[Na_4]^{3+}$ clusters[4] and $[Ag_4Br]^{3+}$ tetrahedra[5] in the parent aluminosilicate sodalite.

Group VI (S, Se, and Te) phosphors are particularly attractive in terms of their demonstrated efficiency, visible and ultraviolet wavelength accessibility, and variable luminescence lifetimes. Primarily for these reasons, chemists and materials scientists first examined quantum-confined semiconductors with studies of small-particle ZnS and CdS powders.[6] Various synthetic techniques have been employed, with relative degrees of success, for particle size control of group VI based clusters during synthesis, including diffusion control of reactants, cluster surface passivation or

[†] Current address: Department of Chemical Engineering and Materials Science, University of Minnesota, 421 Washington Ave. S.E., Minneapolis, MN 55455.

[‡] Address: Department of Chemistry, University of Western Australia, Nedlands, WA 6907, Australia.

[§] Current address: Paul Scherrer Institute, CH-5232 Villigen PSI, Switzerland.

[⊥] Current address: Phytomed Armand Kilchherr, CH-3415 Halse-Rüegsau, Switzerland.

[∥] Current address: Institut für Anorganische Chemie, Ludwig-Maximilians-Universität, D-80333 München, Germany.

[⊗] Abstract published in *Advance ACS Abstracts,* August 1, 1996.

(1) Seel, F. In *Studies in Inorganic Chemistry*; Muller, A., Krebs, B., Eds.; Elsevier Science Publishers B. V.: Amsterdam, 1984; pp 67−89.

(2) Faughnan, B. W.; Heyman, P. M.; Gorog, I.; Shidlovsky, I. In *Advances in Image Pickup and Display*; Academic Press: New York, 1981, Vol. 4, pp 87−155. See also: Blake, N. P.; Srdanov, V. I.; Stucky, G. D.; Metiu, H. *J. Chem. Phys.* **1996**, *104*, 8721 and included references.

(3) Tranjan, F. M.; Todd, L. T. *J. Electrochem. Soc.* **1988**, *135*, 2288−91.

(4) Srdanov, V. I.; Haug, K.; Metiu, H.; Stucky, G. D. *J. Phys. Chem.* **1992**, *96*, 9039−9043. Nenoff, T. M.; Harrison, W. T. A.; Gier, T. E.; Keder, N. L.; Zaremba, C. M.; Srdanov, V. I.; Nicol, J. M.; Stucky, G. D. *Inorg. Chem.* **1994**, *33*, 2472−8.

(5) Stein, A.; Macdonald, P. M.; Ozin, G. A.; Stucky, G. D. *J. Am. Chem. Soc.* **1990**, *112*, 904−905. Ozin, G. A.; Kuperman, A.; Stein, A. *Angew. Chem., Int. Ed. Engl.* **1989**, *28*, 359−376.

(6) Papavassiliou, G. C. *J. Solid State Chem.* **1981**, *40*, 330−335.

S0897-4756(96)00168-8 CCC: $12.00

"capping" with various ligands, formation of nanoclusters in reversed micelles, and inclusion in solid hosts such as glasses or zeolites.[7−9] Solution growth of nanocluster particles[10] and their assembly into 3-D ordered arrays of colloidal crystals[11] has evolved to the point that there is now excellent control over particle size dispersion.

Inclusion within crystalline hosts such as zeolites provides an alternative mechanism for creating periodic 3-D cluster assemblies.[12] If nanoclusters of precisely uniform particle size and composition can be created in the crystalline zeolite cages, one can potentially obtain well-defined relationships between structural and electronic properties, by modifying the sodalite framework to control cage potential, cluster size, intercluster coupling, and periodicity.

The sodalite cage structure consists of a three-dimensional, cubic close-packed array of face-sharing cuboctahedral "cages" supported by framework charge-balancing intracage tetrahedra. The most general composition of the cubic sodalite unit cell is $M_8X_2[TO_2]_{12}$, in which tetrahedral atoms, T, linked by bridging oxygen atoms, form the anionic framework that encloses $[M_4X]^{6+}$ tetrahedra yielding the structure with $I\bar{4}3m$ symmetry. The framework tetrahedral atoms can be substituted to generate the cubic sodalite with $P\bar{4}3n$ symmetry and general composition $M_8X_2[T_1T_2O_4]_6$, in which the T_1 and T_2 atoms are perfectly ordered, as shown schematically in Figure 1. Many sodalite analogues with a wide range of M, X, and T anionic groups or atoms are known.[13]

Smith and co-workers[14] first reported the structure of the borate sodalite analogue $Zn_8O_2[BO_2]_{12}$ based on crystals grown by the Czochralski technique, and Fouassier et al.[15] synthesized the powder analogues $Zn_8X_2[BO_2]_{12}$ (X = O, S, Se). Meijerink and co-workers[16] reported that after UV excitation, single-crystal $Zn_8O_2[BO_2]_{12}$ exhibits a violet emission with a strong afterglow. The violet emission was ascribed to the direct recombination of some of the UV-induced free charge carriers and the large observed Stokes shift (ca. 2 eV) to appreciable lattice relaxation (phonon coupling). The afterglow, or thermoluminescence, was attributed to the recombination of charge carriers trapped at thermally unstable sites in the structure. On the basis of temperature-dependent EPR and glow curve measurements, they assigned the radiation-induced paramagnetic centers that give rise to the observed thermoluminescence bands (in order of increasing thermal stability) to electrons trapped at cage center vacancies, at or near Mn^{2+} impurities, and at framework oxygen vacancies.

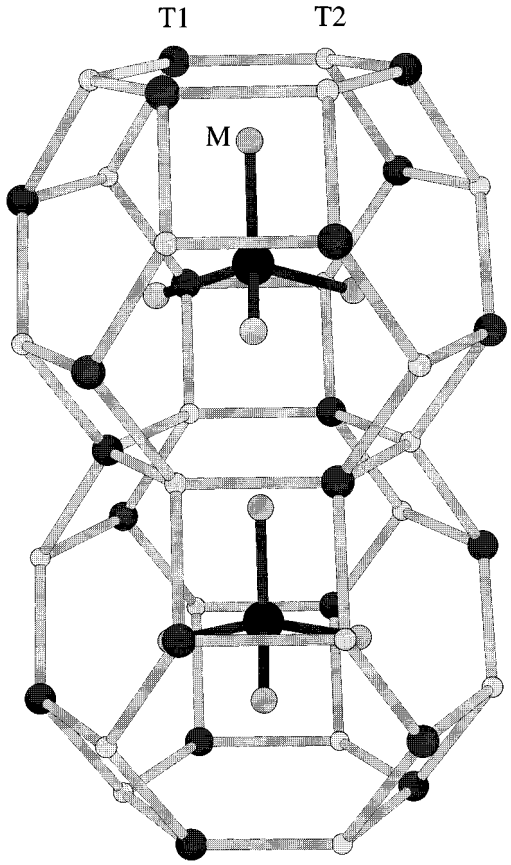

Figure 1. Schematic diagram of the sodalite structure with general formula $M_8X_2[T1T2O_4]_6$. The large sphere at the center of each cage is the anion, X, surrounded tetrahedrally by four cations, M. The ordered tetrahedral framework atoms, T1 and T2, are represented as vertexes in the framework bridged by oxygen atoms, which are not shown. The cations are directed toward the 6-ring faces of the cuboctahedral cages.

The group of sodalite analogues with general composition $M_8X_2[BeSiO_4]_6$ are known as the helvites or helvines (M = Mn), danalites (M = Fe) and genthelvites (M = Zn), and single-crystal studies of these $P\bar{4}3n$ sodalites have been limited to the natural minerals.[17] Fursenko[18] reported the synthesis of $(Mn,Fe,Zn)_8S_2[BeSiO_4]_6$ solid solutions grown under hydrothermal conditions, and Mel'nikov and co-workers[19] reported successful hydrothermal growth of good-quality crystals of the series $M_8X_2[Be(Si,Ge)O_4]_6$ (M = Cd, Zn, Mn; X = S, Se, Te). They measured the unit-cell parameters

(7) See: Steigerwald, M. L.; Brus, L. E. *Annu. Rev. Mater. Sci.* **1989**, *19*, 471−495, for a review.
(8) Stucky, G. D.; Srdanov, V. I.; Harrison, W. T. A.; Gier, T. E.; Keder, N. L.; Moran, K. L.; Haug, K.; Metiu, H. I. In *Supramolecular Architecture*; Bein, T., Ed.; ACS Symposium Series 499; American Chemical Society: Washington, DC, 1992; pp 294−313.
(9) Brus, L. E. *J. Phys. Chem.* **1986**, *90*, 2555−2560.
(10) Steigerwald, M. L.; Alivisatos, A. P.; Gibson, J. M.; Harris, T. D.; Kortran, R.; Muller, A. J.; Thayer, A. M.; Duncan, T. M.; Douglass, D. C.; Brus, L. E. *J. Am. Chem. Soc.* **1988**, *110*, 3046−3050.
(11) Vossmeyer, T.; Katsikas, L.; Giersig, M.; Popovix, I. G.; et al. *J. Phys. Chem.* **1994**, *98*, 7665−7673. Murray, C. B.; Norris, D. J.; Bawendi, M. G. *J. Am. Chem. Soc.* **1993**, *115*, 8706−8715. Murray, C. B.; Kagan, C. R.; Bawendi, M. G. *Science* **1995**, *270*, 1335−1338.
(12) Wang, Y.; Herron, N. *J. Phys. Chem.* **1988**, *92*, 4988. Herron, N.; Wang, Y.; Eddy, M. M.; Stucky, G. D.; Cox, D. E.; Moller, K.; Bein, T. *J. Am. Chem. Soc.* **1989**, *111*, 530. Stucky, G. D.; MacDougall, J. E. *Science* **1990**, *247*, 669. Ozin, G. A.; Steele, M. R. *Adv. Mater.* **1994**, *6*, 300.
(13) See, for example: Taylor, D. *Contrib. Mineral. Petrol.* **1967**, *16*, 172−188. Schnick, W.; Lücke, J. *Angew. Chem., Int. Ed. Engl.* **1992**, *31*, 213−215.
(14) Smith, P.; Garcia-Blanco, S.; Rivoir, L. *Z. Kristallogr.* **1964**, *119*, 375−383. Smith-Verdier, P.; Garcia-Blanco, S. *Z. Kristallogr.* **1980**, *151*, 175−177.
(15) Fouassier, C.; Levasseur, A.; Joubert, J. C.; Muller, J.; Hagenmuller, P. *Z. Anorg. Allg. Chem.* **1970**, *375*, 202−208. Levasseur, A.; Rouby, B.; Fouassier, C. *C. R. Acad. Sci. Paris* **1973**, *277*, 421−423.
(16) Meijerink, A.; Blasse, G.; Glasbeek, M. *J. Phys.: Condens. Matter* **1990**, *2*, 6303−6313.
(17) Pauling, L. *Z. Kristallogr.* **1930**, *74*, 213−225. Hassan, I.; Grundy, H. D. *Am. Mineral.* **1985**, *70*, 186−192. Dunn, P. J. *Miner. Mag.* **1976**, *40*, 627−636. Holloway, Jr., W. M.; Giordano, T. J.; Peacor, D. R. *Acta Crystallogr.* **1972**, *B28*, 114−117.
(18) Fursenko, D. A. *Fiz-Khim. Issled. Mineraloobraz. Sist.* **1982**, 104−107.
(19) Mel'nikov, O. K.; Litvin, B. N.; Fedosova, S. P. In *Hydrothermal Synthesis of Crystals*; Lobachev, A. N., Ed.; Consultants Bureau: New York, 1971; pp 119−125.

from powder XRD data of the ground crystals and, although up to five crystallographically distinct phases were obtained in some cases, only the desired helvite phase was identified and the crystals were not otherwise characterized.

Previously we reported the inclusion of $[Zn_3GaP]^{6+}$ and $[Zn_4Se]^{6+}$ in the borate sodalite framework.[20] On the basis of powder XRD, UV/vis, and ^{31}P MAS NMR data, we concluded that the sodalite framework isolates the intracage tetrahedra electronically and magnetically, resulting in an isolated $^{69,71}Ga$, ^{31}P spin pair and a strong blue shift in the UV/vis absorption relative to the bulk semiconductors. Brenchley and Weller[21] investigated the structure and optical properties of $[Cd_4S]^{6+}$ included in the aluminate sodalite analogue and reported a dramatic high-energy shift in the optical absorption of the material, relative to the bulk semiconductor.

In this paper, we report for the first time an investigation of how cage size and potential properties can be used to systematically modify electronic and optical properties of guest clusters incorporated within a zeolite cage. The composition-dependent structural, electronic, and optical properties of the solid solutions series $Zn_8X_2[BO_2]_{12}$ (X = O, S, Se) and $[Cd_yZn_{1-y}]_8X_2[BeSi_xGe_{1-x}O_4]_6$ (X = S, Se, or Te) are presented. The materials are characterized by powder and single-crystal X-ray diffraction studies and by multinuclear solid-state MAS NMR, CdL_3 XANES, UV/visible diffuse reflectance, and photoluminescence spectroscopic measurements. Additionally we report the first structural analyses of synthetic helvite single crystals and compare the optical properties with those of the as-synthesized powder analogues.

Experimental Section

Materials. Electronic grade zinc and cadmium chalcogenides and main-group oxides were purchased from Alfa or Strem, and all other reagents were purchased from Fisher. All starting materials were heated to constant mass (maximum of 200 °C for the chalcogenides, 400 °C for the oxides) to remove physisorbed water prior to mixing. High surface area BeO was prepared by dehydrating $Be(OH)_2$ at 400 °C. Preparation of a starting material of nominal stoichiometry ZnB_2O_4 was a convenient method for simultaneously dehydrating ZnO and H_3BO_3. To avoid contact with the highly toxic beryllium, cadmium, and chalcogenide compounds, these materials were handled in a Plexiglas glovebox within a fumehood and full personal protection was worn, including a fitted respirator with type H cartridges (Sparkfoe, from Fisher).

Synthesis. The borate sodalites were synthesized as described previously.[22] $Zn_8O_2[BO_2]_{12}$ was prepared hydrothermally from a 4:1 molar ratio of H_3BO_3 and ZnO in water, sealed in a Teflon pouch and heated in an autoclave for 4 days at 150 °C, 80 psi (54 atm). The sulfide and selenide analogues, which are hydrolyzed under the mildly acidic hydrothermal conditions, were prepared by solid-state reaction. Stoichiometric mixtures of the dehydrated oxides and chalcogenide (typically ~1 g total mass) were ground together finely with a mortar and pestle, loaded into graphite-coated quartz ampules and flame-sealed under vacuum (10^{-3} Torr). Sealed quartz ampules were secured inside steel tubes with Fiberfrax (Lindberg) as containment devices in case of ampule failure, placed in a cold muffle furnace, heated over a slow ramp (ca. 6 h), and then held at 900 °C for 12−72 h. Ampules were removed from the muffle furnace at room temperature and opened cautiously. The beryllosilicates and -germanates were prepared by an analogous procedure from finely ground stoichiometric mixtures of dry, nonrefractory reactants sealed under vacuum in *untreated* quartz ampules and heated at 800 °C for at least 12 h. All products were recovered as homogeneously colored, free-flowing powders.

Single crystals were prepared from the powder helvites with starting stoichiometries of $Zn_8S_2[BeSi_xGe_{1-x}O_4]_6$, $x = 0$, 0.33, and 0.67. The as-synthesized powders were mixed with 3% NaOH solution, flame-sealed in gold tubes, and positioned inside a high-temperature, high-pressure bomb (TemPres) filled with water. A maximum reaction temperature of 600 °C at 45 000 psi (3062 atm) was maintained for 5 days, and then the bomb was cooled at a rate of less than 4 °C/h.[23] Products were filtered and washed with water, and in most cases at least two phases were identified: recovered powders generally contained bulk ZnS along with the helvite phase and long needles (identified as Na_2ZnGeO_4 and related NASICON structures) were recovered with helvite single crystals. A large, well-formed translucent sodalite crystal was selected at each stoichiometry for analysis.

Characterization. Elemental analysis was performed by Galbraith Laboratories, Inc. (Knoxville, TN) on samples washed in an oxidizing solution.[24] The calculated analysis for $Zn_8S_2[BO_2]_{12}$ (in mass percent) is 5.82 S, 11.78 B, and 47.51 Zn; found 5.43 S, 13.17 B, and 48.32 Zn. The calculated analysis for $Zn_8SSe[BO_2]_{12}$ (in mass percent) is 2.79 S, 6.88 Se, and 45.57 Zn; found 2.53 S, 6.67 Se, and 45.65 Zn.

Excess Bulk Semiconductor. Although the single-crystal sodalite analogues are single phase, all the powder sodalites examined in this study contain the corresponding bulk semiconductor as a minor phase. All the recovered mixed intracage cation (Cd, Zn) sodalites contain a separate phase identified as the bulk cadmium chalcogenide although many had been prepared with CdO and the bulk zinc chalcogenides; evidently the II−VI compound and CdO metathesize during synthesis. Powder XRD is considerably less sensitive than UV/vis reflectance spectroscopy to bulk semiconductor dispersed in a polycrystalline mixture. For example, we measured the powder XRD patterns and UV/vis spectra of bulk sphalerite ZnS and $MgCO_3$ physical mixtures. The (111) diffraction peak of ZnS ($d = 3.13$ Å) was absent in XRD patterns of mixtures less than 3% ZnS by mass. In contrast, the absorption band onset of bulk ZnS at 350 nm (measured at the midpoint of the absorption curve) was readily detected in the UV/vis spectra of mixtures as low as 0.1% ZnS. Where detectable in the sodalite powders examined in this study, the bulk semiconductor XRD peaks are sharp, consistent with large particle sizes.

The properties of the sodalite analogues are readily distinguished from those of the residual bulk semiconductor in the NMR and photoluminescence spectra of the powders. The UV/visible spectra of the powders are sensitive to the residual material, however: optical absorption of the bulk semiconductor is evident at higher wavelength and due to its large density of states, its absorption band extends beyond that of the powder sodalite analogue, precluding accurate measurement of the latter. Attempted syntheses of the borate sodalite analogues with a stoichiometric deficiency of the II−VI compounds resulted in the formation of $Zn_8O_2[BO_2]_{12}$ along with the desired chalcogenide sodalite phase and residual bulk semiconductor. For the beryllosilicates and -germanates, a stoichiometric deficiency of the bulk II−VI compound resulted in either no appreciable improvement in phase purity or the

(20) Moran, K. L.; Gier, T. E.; Harrison, W. T. A.; Stucky, G. D.; Eckert, H.; Eichele, K.; Wasylishen, R. E. *J. Am. Chem. Soc.* **1993**, *115*, 10553−10558.

(21) Brenchley, M. E.; Weller, M. T. *Angew. Chem., Int. Ed. Engl.* **1993**, *32*, 1663−1665.

(22) Moran, K. L.; Harrison, W. T. A.; Gier, T. E.; MacDougall, J. E.; Stucky, G. D. *Mat. Res. Soc. Symp. Proc.*; Materials Research Society: Pittsburgh, 1990; Vol. 164, pp 123−128.

(23) We synthesized the CdS analogues using the same procedure. Due to the affinity for gold of the selenides and tellurides, however, these hydrothermal syntheses were not possible with our equipment. Mel'nikov and co-workers[19] used titanium containers for successful growth of all the helvite analogues.

(24) The powders were stirred for at least 12 h in an aqueous solution of Br_2 adjusted to pH 6 with hypochlorite solution (bleach).

Table 1. Crystallographic Parameters for Single Crystals of Composition $Zn_8S_2[BeGe_{1-x}Si_xO_4]_6$[a]

empirical formula	$Zn_8S_2Be_6Ge_{5.82}Si_{0.18}O_{24}$	$Zn_8S_2Be_6Ge_{3.77}Si_{2.23}O_{24}$	$Zn_8S_2Be_6Ge_{1.56}Si_{4.44}O_{24}$
mole fraction of Si, x	0.03	0.37	0.74
formula weight	1460.69	1371.68	1260.42
color and habit	clear tetrahedron	clear tetrahedron	clear thick plate
crystal size (mm^3)	0.35 × 0.35 × 0.35	0.25 × 0.25 × 0.25	0.35 × 0.35 × 0.10
crystal system	cubic	cubic	cubic
a (Å)	8.250(4)	8.221(2)	8.163(1)
V (Å)	561.5(8)	555.6(4)	543.9(2)
Z	1	1	1
space group	P23 (#195)	P23 (#195)	P23 (#195)
T (°C)	20	20	20
ρ_{calc} (g/cm^3)	4.319	4.099	3.848
λ(Mo Kα) (Å)	0.71073	0.71073	0.71073
μ(Mo Ka) (cm^{-1})	166.835	143.466	114.45
hkl data limits	0<h<8, 0<k<8, 0<1<8	0<h<8, 0<k<8, 0<1<8	0<h<8, 0<k<8, 0<1<8
maximum 2θ	45°	45°	45°
total data	464	464	458
unique data	158	158	156
$R_{int}(I)$	5.33%	4.14%	2.84%
obsd data $I > 3\sigma(I)$	148	151	153
parameters	27	27	27
$R(F)$	2.82%	2.19%	2.33%
$R_w(F)$	3.98%	2.30%	3.92%
GOF	0.88	0.80	0.79

[a] $R = \sum||F_o| - |F_c||/\sum|F_o|$, $R_w = [\sum(|F_o| - |F_c|)^2/\sum w|F_o|^2]^{1/2}$, with w defined by a Tukey Prince-type weighting scheme, with Chebychev coefficients of 18.8, 3.55, 10.6. Formula weight, ρ_{calc} (g/cm^3) and μ(Mo Kα) (cm^{-1}) are calculated assuming $x = 0$.

formation of Zn_2SiO_4 (willemite phase), isomorphous Zn_2GeO_4, cadmium silicate or germanate in addition to the sodalite phase. Attempted selective dissolution of the bulk semiconductor[25] was partially successful in the borate sodalite phase mixtures, whereas attempted selective oxidation by heat treatment[25] was not successful. Due to the toxicity of the beryllosilicates and -germanates, handling of the powders was minimized and postsynthesis removal of the bulk semiconductor was not attempted.

Structural Characterization. Powder XRD data were collected with a Scintag PAD-X $\theta-\theta$ powder diffractometer using Cu Kα radiation ($\lambda = 1.5418$ Å) with Si as an internal standard. High-resolution powder XRD data for Rietveld analyses were collected over 12-h periods from $2\theta = 10-80°$, with a typical step size of 0.02°. Synchrotron source powder diffraction data ($\kappa = 0.7009$ Å) were collected for the cadmium beryllosilicates to minimize absorption effects due to cadmium.

The structures of the borate sodalites were refined in space group $I\bar{4}3m$, as described previously.[23] The structures of the beryllosilicates and -germanates were refined in space group $P\bar{4}3n$ using the structure of aluminosilicate hydroxy sodalite as a starting model.[26] With the program GSAS,[27] the zero-point correction, background coefficients, lattice parameter, and atomic positions were refined, and then isotropic thermal parameters and peak-shape descriptors were added progressively until refinements converged to satisfactory χ^2 values, Bragg R factors, and visual fit. The profile R factors obtained were generally 12% or less, although heavy-atom compositions tended to give higher values (less than 20% for $Cd_8Se_2[BeGeO_4]_6$ and $Cd_8Te_2[BeGeO_4]_6$). There are many views about the best way to judge the quality of fit in a Rietveld refinement. R values can be very misleading because they are dramatically influenced by the background and it is even possible to get low profile R factors (~3%) by fitting the backgrounds without a very good fit to the Bragg peaks if the background is high. Heavy-atom scatterers increase the background making it more difficult to get good Bragg peak fits. The χ^2 test gives a somewhat better indication but can also be misleading for the same reason. The Bragg R factors and the visual fit to the data are perhaps the best guides.[28]

Refinement of the mixed intracage (Cd,Zn) helvites by constraining the Cd:Zn ratio or by setting the Cd:Zn ratio based on a Vegard's law calculation led to different Cd:Zn ratios (7:1 or 3:1, respectively) but essentially identical residuals ($R(p) = 11.83\%$, $R(wp) = 16.67\%$, $c2 = 1.08$). The assigned Cd:Zn ratio was based on the assumption that the solid solutions obey Vegard's law. The cations in the mixed intracage (Cd,Zn) helvites were fixed as cadmium atoms during refinement and the relative amounts of each were calculated from the unit cell dimensions under the assumption that the solid solutions obey Vegard's law.

Single-Crystal Analyses of $Zn_8S_2[BeSi_xO_4]_6$. A good-quality, translucent crystal at each stoichiometry was selected and mounted on a thin glass fiber with fast-setting epoxy. Intensity data were collected in $\theta/2\theta$ mode on a MicroVaxII-controlled Huber four-circle diffractometer using graphite-monochromated Mo Kα radiation, $\lambda = 0.710\,73$ Å. The cubic unit-cell parameters were determined by least-squares refinement of centered reflections. Intensity data were collected at a rate of 1.5°/min from 1.4° below $K\alpha_1$ to 1.5° above $K\alpha_2$ to a maximum 2θ of 45°. Three intense reflections were monitored every hundred reflections and exhibited negligible intensity fluctuations over the course of the experiment. Prior to refinement, data were corrected for absorption effects by the ψ-scan method and corrected for polarization and Lorentz effects. Inspection of the intensity data revealed the presence of weak reflections that are forbidden by $P\bar{4}3n$ symmetry, those reflections where hhl, $l = 2n + 1$. Therefore the space group $P23$ (No. 195), a subgroup of $P\bar{4}3n$ for which there are no special conditions, was chosen. The structure was solved by heavy-atom methods using SHELXS-86[29] followed by successive difference Fourier methods. Least-squares, Fourier, and subsequent calculations were performed with the Oxford CRYSTALS program.[30] Final full-matrix refinements were against F and include anisotropic thermal parameters for Ge, Si, Zn, and S, secondary extinction correction and Flack chirality parameter.[31] Scattering factors (including anomalous contributions) were taken from International Tables for X-ray

(25) The bulk compounds ZnS and ZnSe are oxidized to ZnO by baking in air at 600 °C for several days. The same treatment of the "contaminated" borate sodalite analogues resulted in no improvement in phase purity. The bulk semiconductors in these phase mixtures were oxidized only after prolonged heating at 800 °C or higher, but this treatment also oxidized the chalcogenide borate sodalites to $Zn_8O_2[BO_2]_{12}$. We suggest that some of the bulk semiconductor particles are coated with B_2O_3 glass early in the reaction, which stabilizes them against subsequent high-temperature oxidation.

(26) Gier, T. E.; Harrison, W. T. A.; Stucky, G. D. *Angew. Chem., Int. Ed. Engl.* **1991**, *30*, 1169−1171.

(27) Larson, A. C.; Von Dreele, R. B. *GSAS Users Guide, Los Alamos Report*; 1988; LAUR 86-748.

(28) *The Rietveld Method*; Young, R. A., Ed.; Chester: England; International Union of Crystallography Monographs on Crystallography (5); Oxford University Press; Oxford, 1993.

(29) Sheldrick, G. M. SHELXS-86 User Guide, Crystallography Department, University of Gottingen, Germany, 1986.

(30) Watkin, D. J.; Carruthers, J. R.; Betteridge, P. W. CRYSTALS User Guide, Chemical Crystallography Laboratory, Oxford, 1985.

Table 2. Experimental Parameters for Single-Pulse MAS NMR Experiments at 7.05 T[a]

nucleus	resonance freq (at 7.05 T)	pulse width (μs)	relaxation delay (min)	ref standard ($\delta = 0$ ppm)
^{9}Be	42.23	4	1	1 M Be^{2+}(aq)
^{11}B	160.45[a]	6	1	BPO_4 ($\delta = -3.3$)
^{29}Si	59.70	7	2	TMS
^{77}Se	57.30	8.5	20	CdSe
^{113}Cd	66.71	5	10	$(CH_3)_2Cd$
^{125}Te	94.74	7	40	CdTe

[a] At magnetic field of 11.7 T.

Crystallography.[32] Parameter shifts in the final least-squares cycle were smaller than 0.03σ. A detailed summary of crystallographic parameters is listed in Table 1.

Spectroscopy. Single pulse MAS NMR spectra were collected on GN-series spectrometers at 7.05 and 11.7 Tesla, using high speed MAS probes manufactured by Doty Scientific, Inc. (Columbia, SC) at sample spinning rates of 3 to 8 kHz. Resonance frequencies, pulse widths, relaxation delays, and chemical shift reference standards are listed in Table 2.

CdL_3 XANES spectra were measured at the storage ring ELSA (Bonn, Germany) at a spectrometer that was equipped with a Si 111 double-crystal monochromator. Spectra were calibrated by simultaneous measurement of the sample spectrum and of the spectrum of a reference ($AgCoO_2$, using the inflection point of the AgL_2 edge for calibration). The samples were prepared as pressed polyethylene pellets. The contents of the Cd sodalites was adjusted to yield an absorption jump $\Delta\mu d$ of about 0.5 at the CdL_3 edge. The preedge background of the spectra was removed and the spectra were normalized applying the usual procedures.

Diffuse Reflectance UV/vis spectra were collected on a Cary 14 monochromator fitted with a $BaSO_4$-coated integrating sphere and upgraded with a computer interface by OLIS, Inc. (Bogart, GA). Powder samples were pressed flat against an optical-quality quartz disk enclosed in a stainless steel holder and spectra were not normalized. $MgCO_3$ was used as the reference standard.

Excitation and emission spectra of the strongly luminescent samples were measured on a Spex Fluorolog in front-face geometry at room temperature and 77 K. Emission spectra of the other powder samples were measured at room temperature with a SpectraPro-500 triple-grating monochromator/spectrograph (Acton Research Corp.) interfaced to a Gateway 2000 Crystal Scan computer, with a 0.2 A, 60 Hz high-intensity UV lamp (Spectroline) as the excitation source. The measured excitation bandwidth was approximately 100 nm centered at 365 nm. Room-temperature excitation and emission spectra of the single crystals were measured on a Spex Fluoromax at the Institut für Anorganische Chemie in Bern, Switzerland. Crystals (approximately 0.1 mm on edge) were mounted on glass fibers with epoxy, and spectra were corrected for the latter.

High-resolution TEM was performed on the single crystal with stoichiometry $Zn_8S_2[BeSi_{0.37}Ge_{0.63}O_4]_6$, crushed in acetone and dispersed on a holey carbon-film-coated copper grid, using a JEOL 1210 (120 kV accelerating voltage) at the Center for Interfacial Engineering, University of Minnesota. Specimens exhibited little or no beam damage. Calculated electron diffraction patterns were generated from refined crystallographic parameters in both *P*43*n* and *P*23 symmetries using the program Cerius2 (Biosym/Molecular Simulations, Inc.).

Results and Discussion

Structural Characterization Based on XRD Results. The zinc borate sodalites and the powder beryllosilicate and -germanate analogues crystallize in the cubic, noncentrosymmetric space groups $I\bar{4}3m$ (No. 217) and $P\bar{4}3n$ (No. 218), respectively. The unit-cell parameters and selected bond distances are listed in Table 3. Final atomic coordinates; *R* factors; observed, calculated, and difference profiles; and complete lists of bond distances and angles are compiled in the supporting information. All the powder helvite refined unit-cell parameters agree with those reported by Mel'nikov et al.,[20] within error, except that of $Cd_8Se_2[BeGeO_4]_6$ (unit-cell length of 8.6314(3) Å compared with the previously reported value of 8.67(0) Å). Inspection of the crystallographic results reveals that within each $[M_4X]^{6+}$ series, the unit-cell dimension, *a*, varies linearly with framework composition, *x* (mole fraction of silicon), and thus the solid solutions obey Vegard's law.

The single crystals of composition $Zn_8S_2[BeSi_xGe_{1-x}O_4]_6$, $x = 0.03$, 0.37, and 0.74, were refined in space group *P*23 (No. 195) due to the presence of weak reflections *hhl*, $l = 2n + 1$, which are not allowed in $P\bar{4}3n$ symmetry. This lower symmetry assignment is supported by selected area electron diffraction of the crushed single crystal with stoichiometry $Zn_8S_2[BeSi_{0.37}Ge_{0.63}O_4]_6$, shown in Figure 2 and compared with the calculated diffraction patterns based on the crystallographic parameters refined in space groups *P*23 and $P\bar{4}3n$. Selected bond distances and angles of the single crystals are listed in Table 4, and atomic coordinates, anisotropic thermal parameters, and observed and calculated structure factors are available as supporting information.

The principal difference between space groups $P\bar{4}3n$ and *P*23 is that in the latter symmetry the sodalite unit cell consists of two crystallographically distinct cages. This symmetry lowering arises primarily from positional siting of the beryllium and two oxygen atoms in the structure; the positional coordinates of the other atoms were constrained during refinement to their respective $P\bar{4}3n$ special positions, as appropriate based on the small positional parameter shifts in both symmetries. Performing the *n*-glide and $\bar{4}$ symmetry operations on the final *P*23 coordinates results in deviations from the "ideal" symmetry locations of 0.038 and 0.057 Å for Be and O, respectively, which is of the same magnitude as the difference between [Ge/Si]−O distances in the Si-rich and Ge-rich crystals (0.091 Å). Thus the deviations of Be and O positions from the ideal $P\bar{4}3n$ symmetry sites is as significant as the structuural effects caused by doping of Si on Ge sites. The [Ge/Si]−O distances, which decrease with increasing Si content, are comparable to "standard" M−O distances calculated by Shannon and Prewitt.[33]

The sodalite framework composition directly affects the extent of contraction and intercage proximities of the included $[M_4X]^{6+}$ tetrahedra. In the $[Zn_4Se]^{6+}$ series, for example, the Zn−Se bond distance is 2.366(2) Å for tetrahedra included in the relatively small borate framework, shorter than that in the bulk sphalerite compound (2.4562(6) Å). When included in the beryllosilicate framework, which yields a larger sodalite unit cell and cage volume, the Zn−Se bond distance is increased to 2.436(4) Å. As germanium is added to the framework, the cage volume increases and the included

(31) Flack, H. *Acta Crystallogr.* **1983**, *A39*, 876−881.
(32) *International Tables for X-ray Crystallography*; Kynoch Press: Birmingham, England, 1974; Vol. IV.
(33) Shannon, R. D.; Prewitt, C. T. *Acta Crystallogr.* **1969**, *B25*, 925−946.

Table 3. Unit-Cell Parameters and Selected Bond Distances of the Sodalite Analogues $M_8X_2[T_{1(x)}T_{2(1-x)}O_4]_6$

framework, composition	mole fraction of Si (x)	unit-cell length, a (Å)	M−X dist (Å)	X−X dist (calcd, Å)	M distance to 6-ring plane (calcd, Å)
		Borates: $Zn_8X_2[BO_2]_{12}$			
X = O		7.4659(3)	1.982(1)	6.4657	1.251
X = S		7.6283(4)	2.262(3)	6.6063	1.041
X = $S_{0.5}Se_{0.5}$		7.665(2)	2.322(2)	6.639	0.998
X = Se		7.6801(4)	2.366(2)	6.6511	0.960
		Helvites: $M_8X_2[BeSi_xGe_{1-x}O_4]_6$			
M = Zn, X = S	1	8.1153(4)	2.346(2)	7.0281	1.168
M = Zn, X = S	0.67	8.170(2)		7.705	
M = Zn, X = S	0.33	8.244(2)		7.140	
M = Zn, X = S	0	8.2696(2)	2.345(3)	7.1617	1.236
M = Zn, X = Se	1	8.1794(3)	2.436(4)	7.0836	1.106
M = Zn, X = Se	0.33	8.284(9)		7.174	
M = Zn, X = Se	0	8.3136(3)	2.449(4)	7.1998	1.151
M = Zn, X = Te	1	8.2677(3)	2.599(4)	7.1600	0.981
M = Zn, X = Te	0	8.4355(9)	2.607(4)	7.3054	1.046
M = Cd, X = S	1	8.41659(3)	2.5001(2)	7.28898	1.1444
M = Cd, X = S	0	8.61011(4)	2.5329(2)	7.45657	1.1954
M = Cd, X = Se	1	8.5053(5)	2.594(5)	7.3658	1.089
M = Cd, X = Se	0.67	8.543(3)		7.398	
M = Cd, X = Se	0.33	8.598(9)		7.446	
M = Cd, X = Se	0	8.6314(3)	2.628(5)	7.4750	1.110
M = Cd, X = Te	1	8.58649(4)	2.7488(2)	7.43612	0.9692
M = Cd, X = Te	0.67	8.620(3)		7.465	
M = Cd, X = Te	0.33	8.691(3)		7.527	
M = Cd, X = Te	0	8.7385(2)	2.765(5)	7.5678	1.019
M = $Cd_{0.75}Zn_{0.25}$; X = Te	0	8.6573(3)	2.695(4)	7.4975	1.054
		Bulk II−VI Compounds			
ZnS		[5.429]	2.351(5)	3.839	
ZnSe		[5.6686]	2.4562(6)	4.008	
ZnTe		[6.101]	2.642(2)	4.314	
CdS		[5.835]	2.527(5)	4.126	
CdSe		[6.05]	2.62(3)	4.28	
CdTe		[6.478]	2.806(2)	4.582	

tetrahedra expand, yielding a Zn−Se bond distance of 2.449(4) Å in the beryllogermanate. The distance between nearest-neighbor $[M_4X]^{6+}$ tetrahedra also increases as the framework is enlarged, and in all the sodalite analogues the intercage anion distance is at least 6.4 Å, a substantially greater distance than the anion−anion separations in the bulk semiconductors.

Within any framework series, inclusion of larger intracage atoms results in a larger unit cell and greater distance between neighboring cage centers. However, the distance from the intracage cation to the plane of the 6-ring window to the adjoining cage (hence the distance to the three closest metal atoms in the adjacent cage) decreases. For example, increasing the size of the cage center anion in the borate sodalites, from S^{2-} to Se^{2-}, enlarges the unit cell size, a, from 7.6283(4) to 7.6801(4) Å, respectively, but the distance from Zn^{2+} to the 6-ring window decreases from 1.041 Å for the sulfide to 0.960 Å for the selenide. The same trend is observed in the helvite sodalite analogues and is most dramatic in the telluride series. The large Te^{2-} anion forces the intracage cations closer to the intercage 6-ring windows than in any of the other helvite analogues examined in this study. A similar effect is observed with increasing intracage cation size: although the included Cd−X bond distances are always greater than those of Zn−X for the same anion in comparable frameworks, the cadmium atoms are closer to adjoining cages than are the corresponding zinc atoms. Thus the rigid sodalite framework does not fully accommodate expansion of the relatively "soft" intracage tetrahedra as larger atoms are included in the structure.

MAS NMR of the Framework Cations. The borate sodalites were examined by ^{11}B MAS NMR and exhibited, in most cases, a small amount of residual ZnB_4O_7 or B_2O_3 glass in addition to the borate sodalite phase. The ZnB_2O_4 starting material consists of four- and three-coordinate boron atoms; the signal due to the four-coordinate boron nucleus is a sharp singlet at 1.2 ppm and the signals due to three-coordinate species form an unresolved structured spectrum centered at about 11 ppm (±0.5 ppm, using BPO_4 as a secondary reference) affected by second-order quadrupole effects. The ^{11}B chemical shifts of the single-phase borate sodalites are 0.0 (±0.5) ppm for all the samples examined.

Similarly, only very subtle trends are detected in the ^{29}Si and ^{9}Be MAS NMR spectra of the helvite framework cations. For example, in the $Zn_8S_2[BeSi_xGe_{1-x}O_4]_6$ solid solution series the ^{29}Si chemical shifts, from −71.1 to −71.6 (±0.5) ppm relative to TMS, are in the range expected for isolated SiO_4^{4-} groups (the so-called Q^0 groups) in minerals.[34] Likewise, the ^{9}Be MAS NMR chemical shifts, from 0.4 ppm in the beryllosilicate to 1.0 ppm in the beryllogermanate (±0.5 ppm, relative to aqueous $Be(NO_3)_2$ solution) are nearly identical within experimental error. As the germanium content of the framework is increased, however, the ^{29}Si MAS NMR line widths increase and the ^{9}Be line widths increase for intermediate composition but are smallest for the solid solution end members. This line width increase at intermediate framework composition indicates general disorder of the framework atoms that is absent in the solid solution end members and may arise from a distribution of isotropic chemical shifts due to the presence of different $Be(OSi)_x(OGe)_{4-x}$ linkages.

(34) Klinowski, J. *Prog. NMR Spectrosc.* **1984**, *16*, 237−309 (a review).

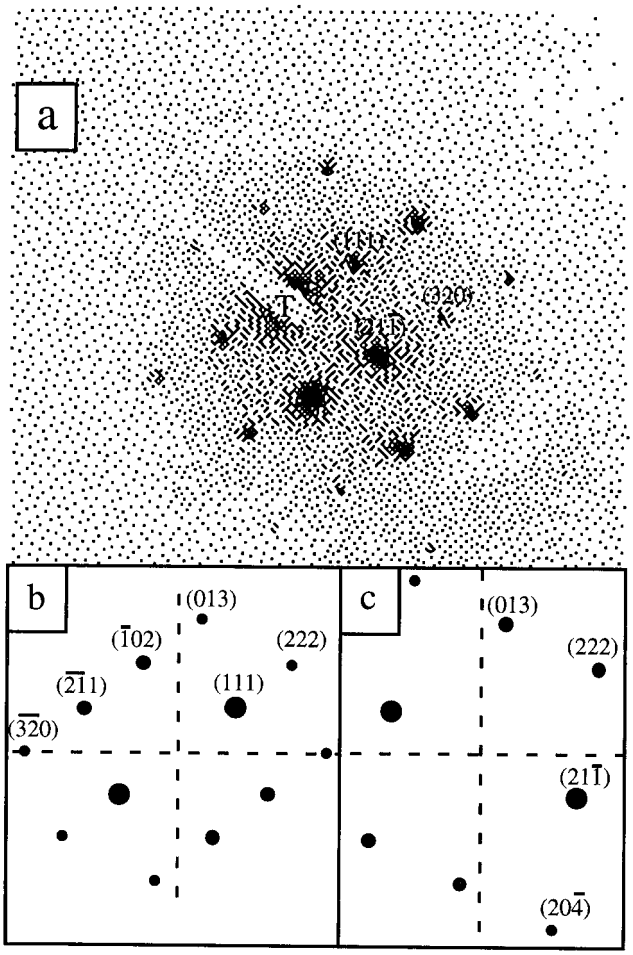

Figure 2. Selected area electron diffraction patterns of $Zn_8S_2[BeSi_xGe_{1-x}O_4]_6$, $x = 0.37$, along the [2$\bar{3}$1] zone axis; (a) experimental pattern, tilted slightly off the zone axis; calculated diffraction patterns generated from refined crystallographic parameters in (b) *P*23 and (c) *P*4$\bar{3}$*n* symmetries.

Table 4. Selected Bond Distances (Å) and Angles (deg) for $Zn_8S_2[BeSi_xGe_{1-x}O_4]_6$

	atomic fraction of Si, *x*		
	0.03	0.37	0.74
Bond Distances (Å)			
Zn(1)−S(1)	2.3445(6)	2.3495(9)	2.348(2)
Zn(2)−S(2)	2.3445(6)	2.3495(9)	2.348(2)
Zn(2)−O(1)	1.974(7)	1.962(4)	1.990(7)
Zn(1)−O(2)	1.971(7)	1.992(5)	1.961(6)
O(1)−[Ge/Si]	1.745(7)	1.716(4)	1.654(7)
O(2)−[Ge/Si]	1.747(8)	1.704(5)	1.666(7)
Bond Angles (deg)			
Zn(1)−S(1)−Zn(1)	109.47(4)	109.47(2)	109.47(4)
Zn(2)−S(2)−Zn(2)	109.47(4)	109.47(2)	109.47(4)
Be(1)−O(1)−Zn(2)	122.3(4)	121.8(2)	119.2(4)
Be(1)−O(2)−Zn(1)	124.3(4)	121.3(3)	119.6(4)
[Ge/Si](1)−O(2)−Zn(1)	116.6(4)	116.6(2)	118.5(4)
[Ge/Si](1)−O(1)−Zn(2)	116.5(4)	117.6(2)	117.5(4)
O(1)−Zn(2)−O(1)	100.9(3)	101.5(1)	101.1(2)
O(2)−Zn(1)−O(2)	103.6(2)	103.5(1)	103.7(2)

^{113}Cd MAS NMR Spectra of the Intracage Cations. The ^{113}Cd MAS NMR spectra of the solid solution series $Cd_8Te_2[BeSi_xGe_{1-x}O_4]_6$ are shown in Figure 3. The isotropic chemical shift assignments for the end members were based on comparison of spectra measured at two different spinning speeds or by approximation of the center of mass. ^{113}Cd MAS spectra of the mixed intracage cation (Cd,Zn) or mixed framework (Si,Ge) solid solutions consisted of very broad peaks, similar to those shown at b and c in Figure 3, and isotropic chemical shifts were not assigned for these materials.

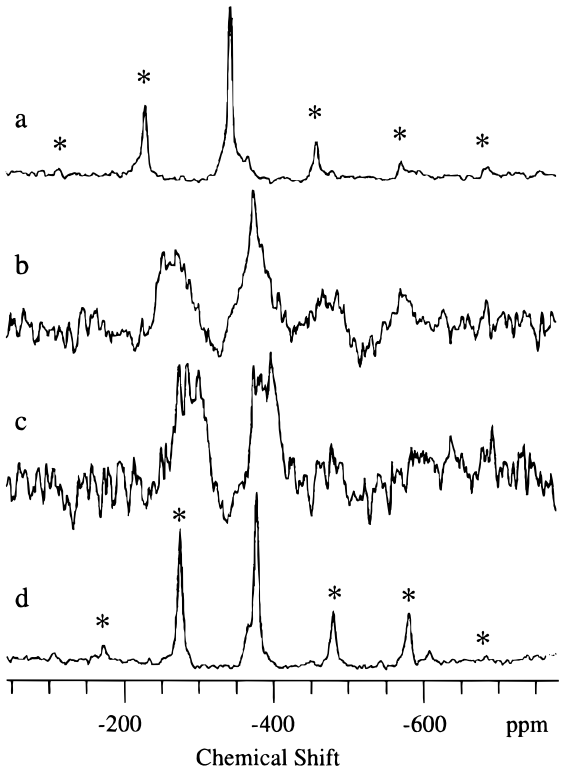

Figure 3. The 66.7 MHz ^{113}Cd MAS NMR spectra of the solid solution series $Cd_8Te_2[BeSi_xGe_{1-x}O_4]_6$; (a) $x = 0$, $\delta = -345$ pp; (b) $x = 0.33$; (c) $x = 0.67$; (d) $x = 1$, $\delta = -380$ ppm, relative to $Cd(CH_3)_2$. Asterisks denote spinning sidebands.

The measured ^{113}Cd isotropic chemical shifts of the solid solution end members $Cd_8Te_2[BeSiO_4]_6$ and $Cd_8Te_2[BeGeO_4]_6$ are −380 and −345 ppm, respectively, shifted to lower and higher resonance frequencies relative to bulk CdTe at −367 ppm (relative to dimethylcadmium). Isotropic chemical shifts of the CdS analogues, on the other hand, are −350 and −322 ppm for the silicate and germanate end members, respectively, shifted to much lower resonance frequency than bulk CdS, at +42 ppm. The ^{113}Cd MAS spectra of the CdSe sodalite analogues consist of substantially broader peaks, suggesting structural disorder of the cadmium atoms. Additionally, the beryllogermanate, at −323 ppm, is shifted to lower frequency relative to the silicate at −295 ppm, contrary to the results obtained for the tellurides and sulfides. Thus there appears to be no direct correlation between the ^{113}Cd MAS chemical shifts and the composition of the sodalite analogues.

The similarities in the ^{113}Cd MAS NMR chemical shifts of the CdS and CdTe helvite analogues, compared with the large chemical shift difference between the corresponding bulk sphalerite semiconductors, suggests that the cage center anion has less influence on the electronic structure of the intracage cation than does the sodalite framework. This is expected because, in the helvite structure, the first coordination sphere about the cadmium nucleus consists of three framework oxygen atoms and the chalcogenide cage center. The envelope of spinning sidebands in the ^{113}Cd MAS spectra reveals an approximately axially symmetric chemical shift tensor, reflecting the lack of cubic symmetry about the intracage cation.

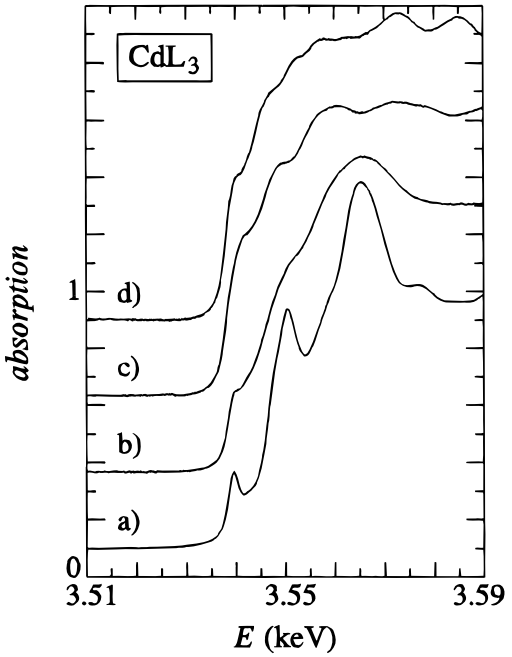

Figure 4. CdL_3 XANES spectra of bulk cadmium chalcogenides: (a) CdO, (b) CdS, (c) CdSe, (d) CdTe.

The preedge region of a XANES spectrum reflects the unoccupied, local electronic structure, selected by the element and the initial state. For spectra measured at the CdL_3 edge, the corresponding signals appear at energies between 3.53 and 3.56 keV. Figure 4 shows the CdL_3 edge spectra of the bulk cadmium chalcogenides. According to Kisiel et al.,[35] who performed band structure calculations of the unoccupied DOS of CdTe, the first signal of spectrum 4d at ∼3.54 keV can be assigned to the $2p_{3/2}\rightarrow 5s$ transition and the second signal at ∼3.55 keV to the $2p_{3/2}\rightarrow 5d$ transition. Note that the corresponding signals of the cadmium chalcogenides in spectra 4a−d exhibit strong differences, corresponding to the differences in electronic structure. Especially, on going from the ionic solid CdO to the semiconductor CdTe, the increasing dispersion of the bands is reflected by the broadening of the preedge peaks.

Figure 5 shows spectra of cadmium helvites. The spectra of the $Cd_8X_2[BeSiO_4]_6$ compounds (Figure 5a−c) are all very similar. In the superposition of the spectra of the sulfide and the selenide (Figure 5e is a superposition of the spectra from 5a and 5b), hardly any differences are apparent. This indicates that the local electronic structure around the cadmium ions is practically independent of the cage anion. In addition, a comparison between the selenide compounds from the beryllosilicate and the beryllogermanate system (spectra 5b and 5d, respectively; 5f is a superposition of these two spectra) shows that differences between these two spectra are larger than between those of Figure 5e. This even implies that the local electronic structure around the Cd atoms is more sensitive to a change in the element of the second coordination from the sodalite framework than to a change in the first coordination from the cage anion. These results thus agree with those from NMR spectroscopy.

Electronic Structure Based on MAS NMR Spectroscopy of the Cage Center Anions. The ^{125}Te MAS NMR spectra of the $Cd_8Te_2[BeSi_xGe_{1-x}O_4]_6$ solid solution series, shown in Figure 6A, illustrate the electronic

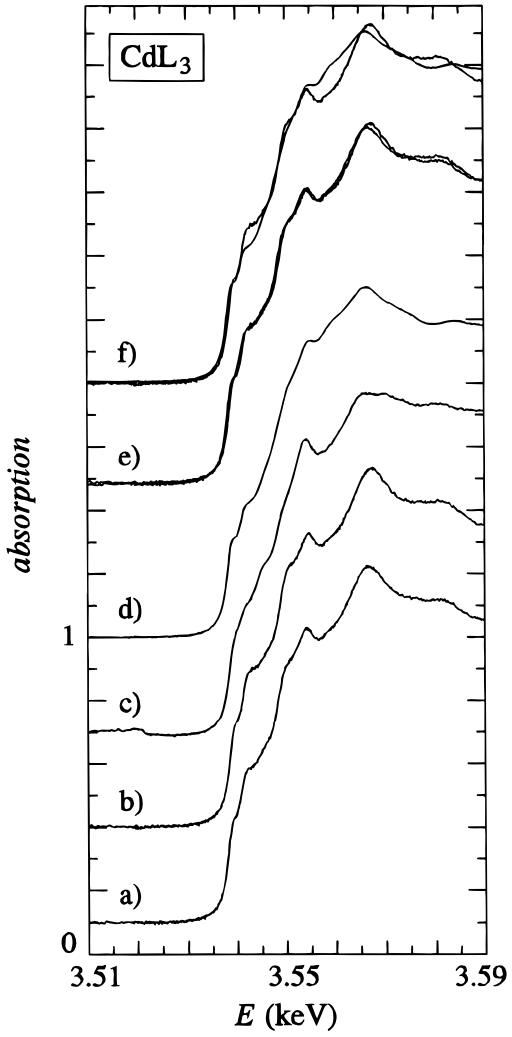

Figure 5. CdL_3 XANES spectra of cadmium beryllosilicate and beryllogermanate sodalites: (a) $Cd_8S_2[BeSiO_4]_6$, (b) $Cd_8Se_2[BeSiO_4]_6$, (c) $Cd_8Te_2[BeSiO_4]_6$, (d) $Cd_8Se_2[BeGeO_4]_6$, (e) superposition of the spectra from (a) and (b), (f) superposition of the spectra from (b) and (d).

localization effect imposed on a semiconductor by inclusion within the sodalite framework. The ^{125}Te MAS NMR resonances are shifted to far lower frequency relative to that of bulk CdTe, the reference compound at 0 ppm. This dramatic low-frequency shift is a consequence of increased diamagnetic shielding and/or a reduced paramagnetic deshielding contribution to the chemical shift.[36] Thus, although the first coordination sphere of the anion is identical with that in the bulk semiconductor, clearly the electronic environment about the tellurium nucleus inside the sodalite cage is significantly different. The discrepancy is ascribed to the charge localization effects imposed on the ^{125}Te nucleus by the extended Te−Te distances; in the bulk semiconductor, nonlocal effects due to charge delocalization over the valence band affect the ^{125}Te resonance. The substantial chemical shift difference between the bulk semiconductor and the helvite analogue facilitates identification of the separate phases in the product

(35) Kisiel, A.; Ali Dahr, A.-I.; Lee, P. M.; Dalba, G.; Fornasini, P.; Burattini, E. *Phys. Rev. B* **1990**, *42*, 11114−11122.

(36) Eckert, H.; Moran, K.; Franke, D.; Hudalla, C. In *Nuclear Magnetic Shieldings and Molecular Structure*; Tossell, J. A., Ed.; *NATO-ASI Series*; Kluwer Academic Publishers: The Netherlands, 1993; Vol. 386, pp 49−73.

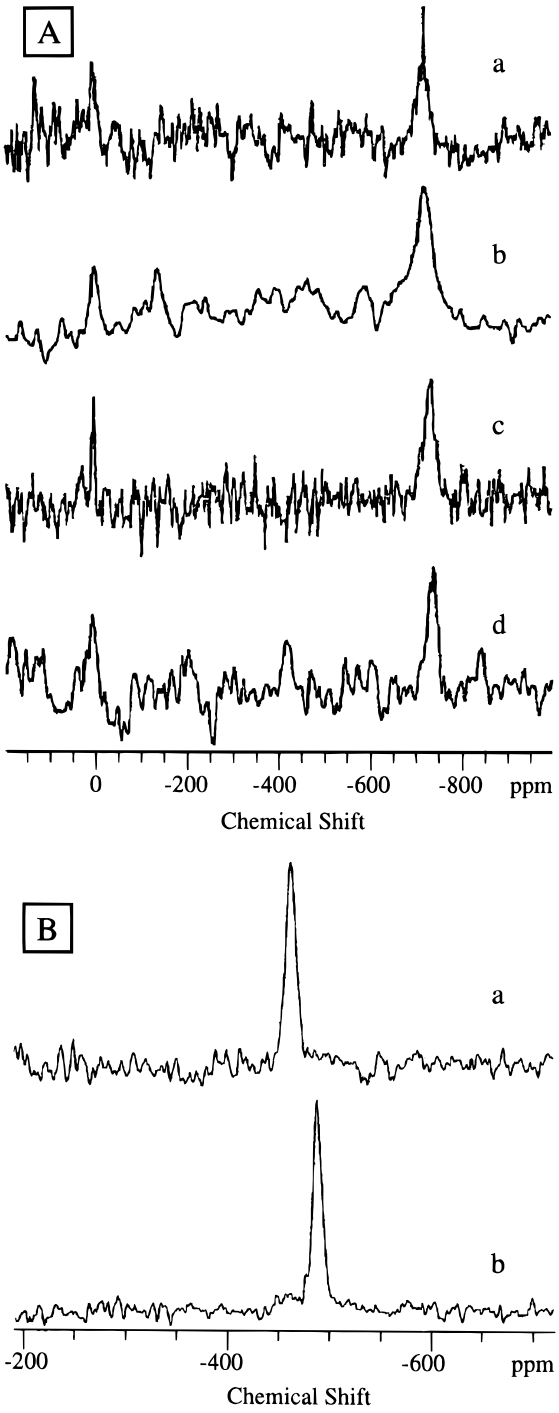

Figure 6. The 94.7 MHz ^{125}Te MAS NMR spectra of (A) the solid solution series $Cd_8Te_2[BeSi_xGe_{1-x}O_4]_6$; (a) $x = 0$, $\delta = -719$ ppm; (b) $x = 0.33$, $\delta = -723$ ppm; (c) $x = 0.67$, $\delta = -731$; (d) $x = 1$, $\delta = -736$ ppm; the sharp peak in each spectrum at 0 ppm is due to residual bulk CdTe. (B) (a) $Zn_8Te_2[BeGeO_4]_6$, $\delta = -466$ ppm and (b) $Zn_8Te_2[BeSiO_4]_6$ $\delta = -491$ ppm.

mixtures. The sharp signal at 0 ppm in each spectrum is due to bulk CdTe; clearly the residual semiconductor is a separate, distinct phase in these mixtures. The ^{125}Te MAS NMR spectra of the ZnTe solid solution end members, in Figure 4B, show an analogous dramatic low-frequency shift relative to bulk ZnTe. Additionally, the effect of the countercation (cadmium vs zinc) on the chemical shift appears to be similar in the helvites and the bulk semiconductors, with the zinc compounds always resonating at higher frequency than the corresponding cadmium compounds. More explicitly, the

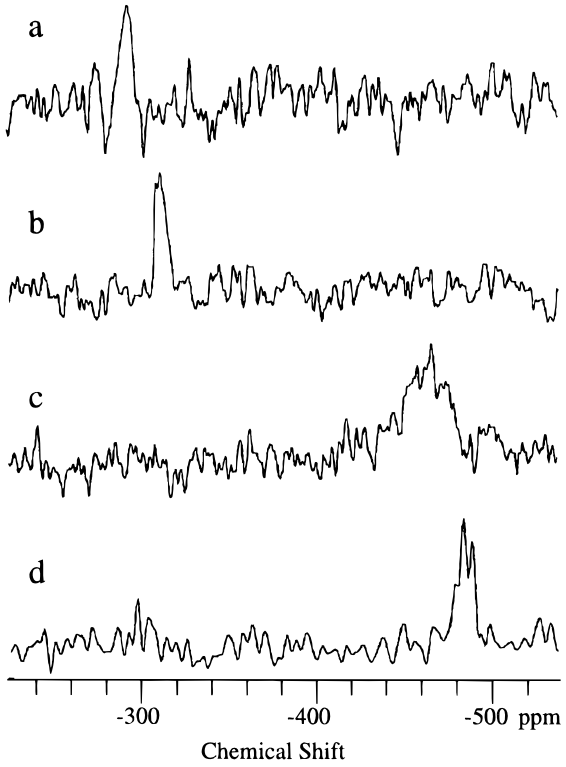

Figure 7. The 57.3 MHz ^{77}Se MAS NMR spectra of (a) $Zn_8Se_2[BeGeO_4]_6$, $\delta = -293$ ppm; (b) $Zn_8Se_2[BeSiO_4]_6$, $\delta = -310$ ppm; (c) $Cd_8Se_2[BeGeO_4]_6$, $\delta = -467$ ppm; (d) $Cd_8Se_2[BeSiO_4]_6$, $\delta = -489$ ppm, all relative to CdSe ($\delta = 0$ ppm).

shift difference of 245 ppm between $Cd_8Te_2[BeSiO_4]_6$ and $Zn_8Te_2[BeSiO_4]_6$, can be compared with the 200 ppm difference between bulk CdTe and ZnTe.

The ^{125}Te MAS NMR spectrum of the crystallographically single-phase, mixed intracage cation helvite analogue, $(Cd_{0.7}Zn_{0.3})_8Te_2[BeGeO_4]_6$, consists of a broad signal centered at -714 ppm (relative to CdTe), thus the electronic environment of the cage center anion in this cadmium-rich helvite more closely resembles the cadmium end member in electronic structure. The substantial broadening of the signal and lack of individual signals attributable to either end member suggests structural disorder about the tellurium nucleus and confirms that the intracage cations are mixed in this material.

The ^{77}Se MAS NMR spectra of the selenide solid solution end members, in Figure 7, are analogous to the ^{125}Te spectra in that they exhibit dramatic low-frequency chemical shifts relative to the corresponding bulk semiconductors. The poor signal-to-noise ratio is the result of the low sensitivity of the ^{77}Se nucleus compounded by long nuclear spin−lattice relaxation times and the low overall selenium content of these samples (12% or less by mass). Despite the poor signal-to-noise ratio, peaks due to scalar coupling between ^{111,113}Cd and ^{77}Se nuclei are discernible in the spectra of $Cd_8Se_2[BeSiO_4]_6$ and $Cd_8Se_2[BeGeO_4]_6$ in Figure 7c,d, respectively. Also analogous to the telluride helvites, the ^{77}Se chemical shift difference between the cadmium and zinc solid solution end members (179 ppm) is increased slightly compared with that of the bulk compounds (124 ppm), suggesting a possibly enhanced cation−anion interaction in the helvites.

For all the sodalite analogues studied, the ^{77}Se and ^{125}Te MAS NMR resonances exhibit rather uniform be-

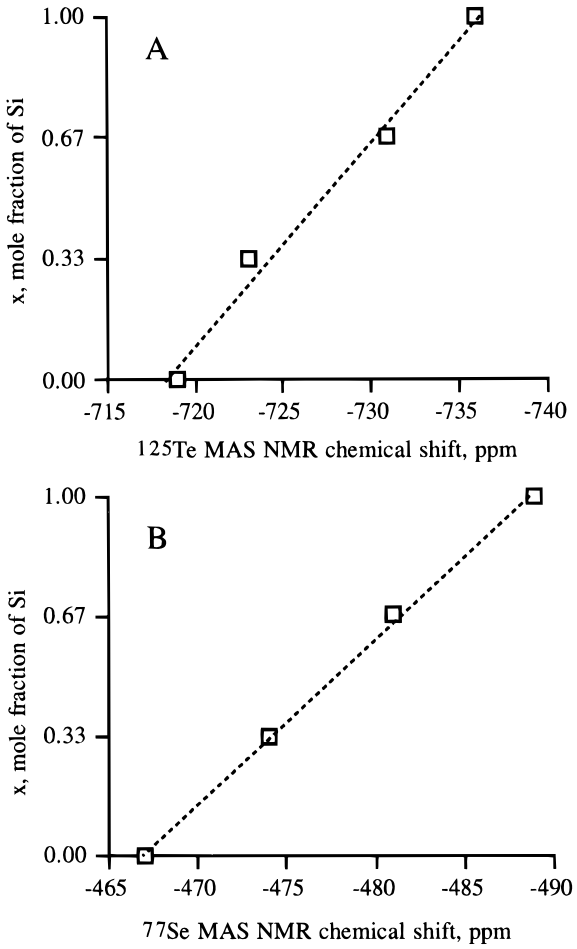

Figure 8. (A) Plot of silicon mole fraction, *x*, versus ^{125}Te MAS NMR chemical shifts of the series $Cd_8Te_2[BeSi_xGe_{1-x}O_4]_6$. (B) Plot of silicon mole fraction, *x*, versus ^{77}Se MAS NMR chemical shifts of the series $Cd_8Se_2[BeSi_xGe_{1-x}O_4]_6$.

havior: the absence of spinning sidebands even when measured at very low spinning speeds illustrates that there are no manifestations of chemical shift anisotropy in these samples, reflecting the strictly cubic point symmetry about the cage center anions. Furthermore, Figure 8 demonstrates that within each telluride and selenide solid solution series, the MAS NMR signal of the cage center anion is shifted linearly to higher frequency as Si is replaced by the larger Ge in the framework; thus there appears to be less electron density localized at the cage center nucleus in the expanded cage. We attribute this trend to the increased M−X distances as the framework germanium content is increased. In the beryllosilicates the intracage tetrahedra are more contracted and the cations are forced closer to the cage center, increasing the electron density at the nucleus. This view is further supported by the ^{77}Se MAS NMR chemical shift of $Zn_8Se_2(BO_2)_{12}$ which occurs at the lowest resonance frequency of all Se^{2-} anions studied here: the borate framework provides the smallest unit cell of all the three sodalite species, and the Zn−Se distances are shortest in this material. On the other hand, the ^{77}Se chemical shifts within the $Zn_8S_xSe_{2-x}[BO_2]_{12}$ series are independent of composition within experimental error. This is likely another manifestation of the electronic isolation of the cage centers; the $[Zn_4{}^{77}Se]^{6+}$ intracage tetrahedra apparently are unaffected by the chemical nature of tetrahedra in

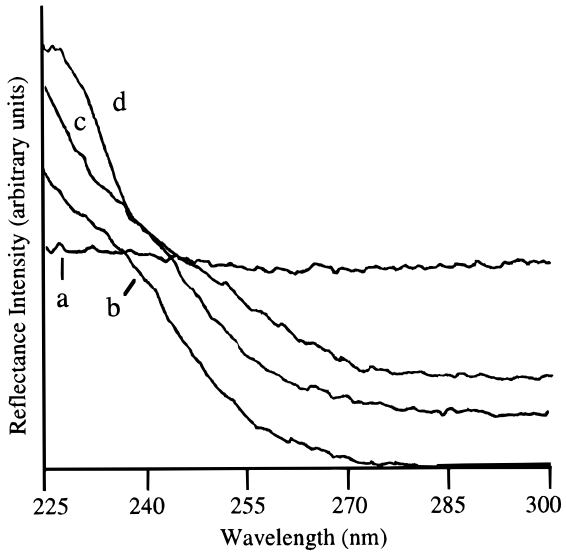

Figure 9. UV/vis diffuse reflectance spectra of the series $Zn_8S_2[BeSi_xGe_{1-x}O_4]_6$: (a) 1.0; (b) $x = 0.33$; (c) $x = 0.67$; (d) $x = 0$. Differences in apparent baseline are due to the absorption of varied amounts of residual bulk ZnS, which has a bandgap at 350 nm.

neighboring cages. Previously we showed that the ^{31}P MAS NMR chemical shifts of $[Zn_3GaP]^{6+}$ included in the borate sodalite are independent of neighboring cage contents in the solid solution series $Ga_xZn_{8-x}P_xSe_{2-x}[BO_2]_{12}$.[21]

Overall, apparently there are several additive contributions to the dramatic low-frequency chemical shifts observed for the sodalite analogue cage center anions. First, the anions in adjacent cages are separated from each other by over 6 Å. This large distance, together with the oxygen-rich framework electrostatic barrier, serves to isolate the anions electronically, i.e., to localize electron density at the cage center. These are probably the predominant contributions to the dramatic low-frequency chemical shifts in these materials, relative to the bulk semiconductors. The cage size, as controlled by the sodalite framework composition, has a smaller but measurable effect of shifting the anion resonance to lower frequency as the M−X distance is decreased. With increasing silicon in the framework, the tetrahedra are contracted within the cage, resulting in shorter M−X distances and increased electron density at the anion nucleus, and the NMR signal is shifted to lower frequency relative to the beryllogermanate.

UV/Visible Spectroscopic Results. While it is difficult to measure precisely the absorption edge energies of the powder sodalite analogues, in general the UV/vis spectra indicate that within a particular $[M_4X]^{6+}$ series, the absorption edge increases in energy as the framework silicon content is increased. The spectra of the ZnS helvites, in Figure 9, illustrate this trend. $Zn_8S_2[BeSiO_4]_6$, and all the $ZnS_xSe_{1-x}[BO_2]_{12}$ sodalites, do not exhibit any absorption features that can be assigned to the sodalite analogue within the instrument detection limits of 225−850 nm; we propose that UV absorption occurs at higher energy in these materials. Previously we reported[23] the UV/vis spectra of $Zn_8S_xSe_{2-x}[BO_2]_{12}$ and related sodalites that exhibited a systematic high energy shift in UV/vis absorption edge with increasing *x*, blue-shifted with respect to the bulk semiconductors. Subsequent work (boiling the phase

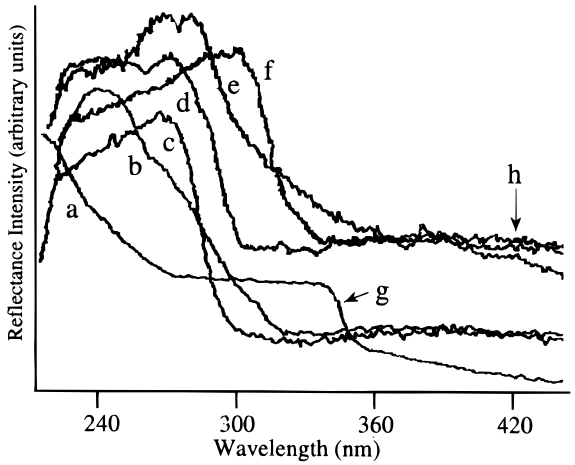

Figure 10. UV/vis diffuse reflectance spectra of the $M_8X_2[BeGeO_4]_6$ solid solution end members, MX = (a) ZnS; (b) ZnSe; (c) ZnTe; (d) CdS; (e) CdSe; (f) CdTe; (g) residual bulk ZnS; (h) absorption due to varied relative amounts of residual bulk semiconductors.

mixtures for several hours in dilute HNO_3, such that most of the sodalite analogue and all of the residual bulk semiconductor were dissolved) revealed that the materials exhibited no UV/vis absorption within our instrument detection limits. We propose that the absorption bands we observed from 340 to 470 nm are most likely due to $Zn_2S_xSe_{2-x}$ alloys that form during the high-temperature borate sodalite synthesis. Previously it has been shown that the direct bandgap energy of $Zn_2S_xSe_{2-x}$ alloys has a nearly linear dependence on x.[37]

The diffuse reflectance spectra of the beryllogermanate solid solution end members, in Figure 10, show that the absorption band edge is a function of the intracage tetrahedra and decreases in energy as the mass of the encaged species increases, analogous but significantly blue-shifted relative to the corresponding bulk semiconductors. The UV/vis absorption energies of the sodalite analogues are listed with the cage center anion MAS NMR chemical shifts in Table 5, and unless otherwise noted, the reported values were measured at the midpoint of the sodalite analogue absorption curve intensity.

Comparison of the UV/vis and MAS NMR spectroscopic data indicate that the latter are a far more sensitive tool for discerning the electronic properties of these materials. Because the NMR signal due to the bulk sphalerite compound is well separated from that of the sodalite, unambiguous measurement of the electronic localization effects is possible. In general there appears to be a correlation between the two sets of spectral data: the lowest wavelength (highest energy) sodalite photon absorption "band" edge corresponds to the lowest frequency anion NMR chemical shift. This correlation between the optical absorption energy, or bandgap, and the NMR chemical shift in semiconductors, originally predicted by Ramsey,[38] is attributed to paramagnetic deshielding of the nucleus due to the angular momenta of excited states mixed in with the ground-state electronic wave function under the influence of the externally applied magnetic field. As the semiconductor particle size is decreased, the incomplete band structure gives rise to an increase in the band gap energy, hence an increase in the average excitation energy, which results in a low-frequency shift in the NMR resonance. This particle-size-dependent low-frequency NMR shift has been experimentally observed in II−VI and III−V semiconductor nanoclusters. For example, Thayer and co-workers[39] reported the ^{77}Se NMR spectra of CdSe clusters, prepared by arrested precipitation, in three different size regimes less than 35 Å. They observed a general low-frequency NMR shift and inhomogeneous broadening of the resonance lines as the size of the nanoclusters was decreased. The line broadening was attributed to a distribution of chemical shifts arising from the different local environments at the surfaces and within the small clusters. Similarly, the ^{31}P and ^{69}Ga MAS NMR spectra of 13 Å GaP clusters included in zeolite NaY exhibit low-frequency shifts relative to bulk GaP and inhomogeneous line broadening, as described by MacDougall et al.[40] In the compounds of the present study, the electronic isolation of the chalcogenide anions may result in both a decreased paramagnetic contribution and an increased diamagnetic contribution to the chemical shift, relative to the bulk semiconductors, thus accounting for the pronounced low-frequency chemical shift effects.

Photoluminescence Spectroscopy of the As-Synthesized Powders. All the $M_8X_2[T_1T_2O_4]_6$ sodalite analogues prepared in this study exhibit photoluminescence after UV excitation; thus there is at least one radiative recombination process whereby the excited state decays. The radiant emission intensity is low for all the materials except the CdTe, ZnTe, and ZnS helvite analogues, which emit intensely enough at room temperature to be visible by the unaided eye. Of these three solid solution series the CdTe helvite analogues are the strongest emitters. The excitation and emission spectra of $Cd_8Te_2[BeGeO_4]_6$ measured at room temperature and 77 K are shown in Figure 11. The room-temperature excitation maximum of 311 nm is slightly blue-shifted and narrowed at 77 K, which is consistent with decreased phonon interactions at the lower temperature. The room-temperature emission spectrum, measured at the excitation maximum of 311 nm, consists of one broad, featureless band centered at 572 nm. This large Stokes shift (261 nm or 1.8 eV) is consistent with considerable phonon interaction after excitation, as was described for the zinc borate analogue.[17] At 77 K, the emission band is blue-shifted, and there are two new emission features: a band centered somewhere to the high-energy side of 400 nm and a lower energy band centered at about 795 nm. These results suggest that after UV excitation, electrons are trapped at three different sites, and only one of these, the trap site corresponding to the center emission band, is thermally stable at room temperature.

The thermally activated detrapping was observed visually in the CdTe helvite analogues. After UV irradiation at 77 K, the visible region emission (corresponding to the emission band centered at approximately 572 nm) decays slowly while the material is at low temperature. Sudden warming of the sample

(37) Bernard, J. E.; Zunger, A. *Phys. Rev. B* **1987**, *36*, 3199−3226.

(38) Ramsey, N. F. *Phys. Rev.* **1950**, *78*, 699−703.

(39) Thayer, A. M.; Steigerwald, M. L.; Duncan, T. M.; Douglass, D. C. *Phys. Rev. Lett.* **1988**, *60*, 2673−2676.

(40) MacDougall, J. E.; Eckert, H.; Stucky, G. D.; Herron, N.; Wang, Y.; Moller, K.; Bein, T.; Cox, D. *J. Am. Chem. Soc.* **1989**, *111*, 8006−8007.

Table 5. Comparison of the Cage Center Anion MAS NMR Chemical Shifts with the Measured Optical Absorption Edge of $M_8X_2[T_{1(x)}T_{2(1-x)}O_4]_6$; M = Cd or Zn; X = ^{77}Se or ^{125}Te

composition: framework, M	X = Se		X = Te	
	^{77}Se MAS NMR shift (±2 ppm)	optical absorption edge (nm)	^{125}Te MAS NMR shift (±1 ppm)	optical absorption edge (nm)
bulk ZnX compound	126	480	200	549
bulk CdX compound	0[a]	512	0[a]	827
$[BO_2]_{12}$ framework, M = Zn	−327 ± 5	<215[b]		
$[BeSi_xGe_{1-x}O_4]_6$ framework:				
M = Zn, x = 1	−310	∼282[c]	−491	245
M = Zn, x = 0.33	−296	271		
M = Zn, x = 0	−293	303	−466	288
M = Cd, x = 1	−489	292	−736	∼336[c]
M = Cd, x = 0.67	−481	301	−731	344
M = Cd, x = 0.33	−474	308	−723	∼344[c]
M = Cd, x = 0	−467	355	−719	∼327[c]

[a] Chemical shift reference. [b] The absorption curve due to the sodalite was not observed within our instrument limits. [c] The midpoint of the sodalite absorption curve was masked by residual bulk semiconductor; thus this is an approximate value.

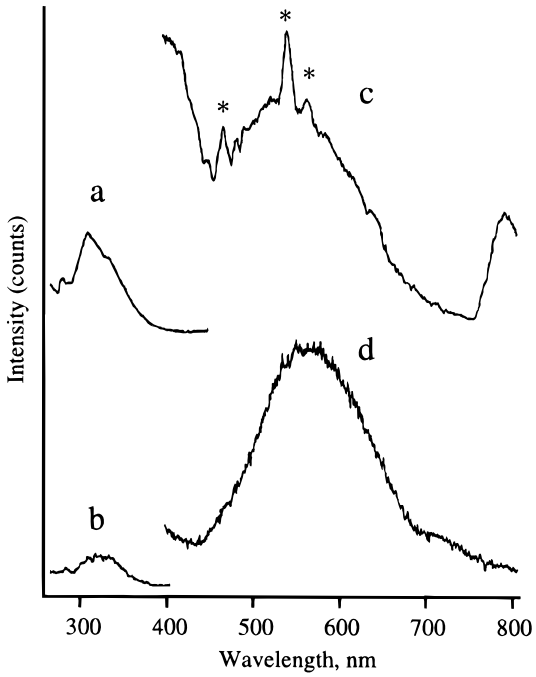

Figure 11. Excitation spectra at (a) 77 K and (b) 298 K; emission spectra at (c) 77 K and (d) 298 K of $Cd_8Te_2[BeGeO_4]_6$. Asterisks denote wavelength positions of lamp artifacts.

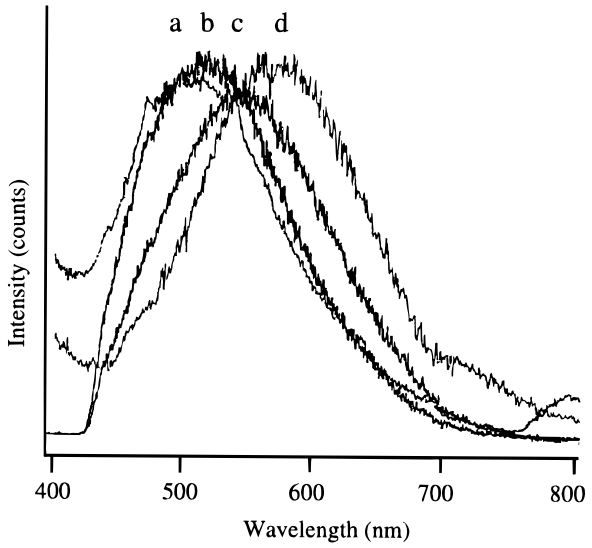

Figure 12. Room-temperature emission spectra of $Cd_8Te_2[BeSi_xGe_{1-x}O_4]_6$: (a) x = 1; (b) x = 0.67; (c) x = 0.33; (d) x = 0. The excitation wavelength is set at the maximum of each corresponding excitation spectrum and intensities are normalized.

produces an intense visible emission at approximately the same color (wavelength) as that observed during irradiation. In the beryllogermanates, which exhibit the most intense visible emission, the effect is dramatic: at 77 K the material can "store" the excitation energy for, at minimum, several minutes.

A comparison of the normalized room temperature emission spectra of the CdTe solid solution series, in Figure 12, shows that the visible region emission energy maxima are directly related to framework composition and thus to the interatomic distances throughout the structure. The room-temperature emission spectra of the zinc and cadmium beryllogermanates and bulk semiconductors, in Figure 13, indicate that the high- and low-energy emission bands are most blue-shifted in the sulfides and most red-shifted in the tellurides, analogous to the trends observed in the UV/vis reflectance spectra. Similarly, the emission bands of the zinc-containing beryllogermanates are blue-shifted with respect to the cadmium members (with the exception of that of $Cd_8Se_2[BeGeO_4]_6$, which may be masked by residual bulk CdSe).

Additionally, the spectra exhibit a difference in relative intensities, or relative quantum yield under identical excitation conditions, as the intracage cation is varied for the same chalcogenide center. Whereas the sulfide-containing beryllogermanate has the most intense emission of the zinc analogues, it has the lowest emission intensity of the cadmium analogues. Likewise, the apparent relative luminescence efficiency shows no correlation for the tellurides or selenides. The markedly lower observed relative emission intensity of all the beryllosilicates suggests that this framework provides a more efficient nonradiative relaxation process or processes, probably due to the smaller interatomic distances throughout the structure. Of the mixed intracage cation helvites prepared in this study, only $[Cd_{0.7}Zn_{0.3}]_8Te_2[BeGeO_4]_6$ luminesces intensely. The room-temperature emission spectrum of this material is shown in Figure 14, with the emission spectra of the CdTe end members included for comparison. Although the mixed intracage cation analogue has a beryllogermanate framework, the emission band maximum is closer in energy to that of $Cd_8Te_2[BeSiO_4]_6$. The emission maximum also is blue-shifted relative to the emission band of $Zn_8Te_2[BeGeO_4]_6$. Apparently the

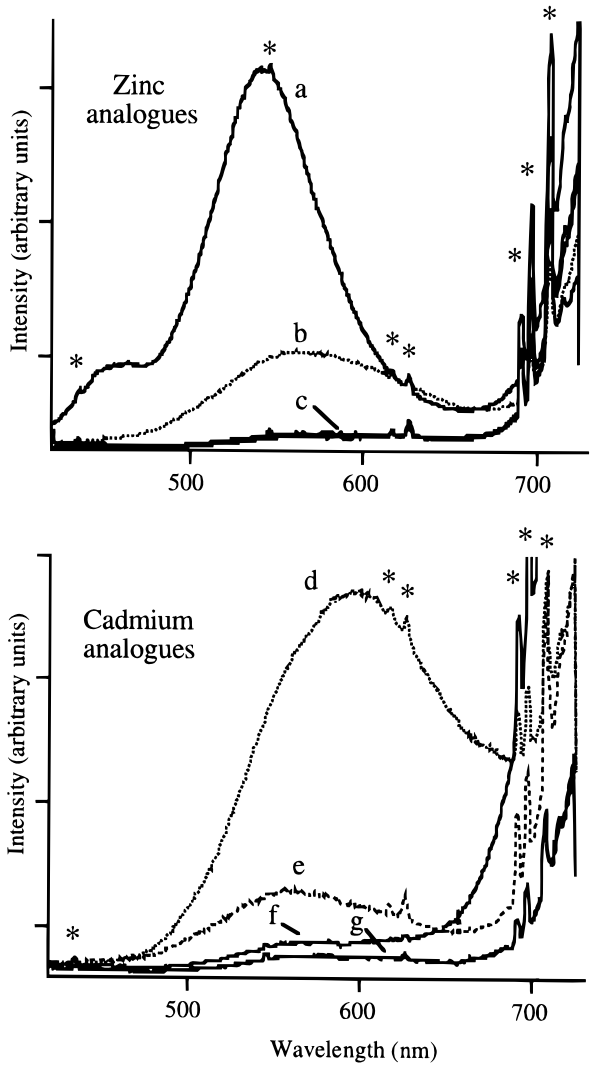

Figure 13. Room-temperature emission spectra of the $M_8X_2[BeGeO_4]_6$ solid solution end members, under broad-band excitation at 365 ± 50 nm of equal sample volumes: (top) (a) $Zn_8S_2[BeGeO_4]_6$; (b) $Zn_8Te_2[BeGeO_4]_6$; (c) coincident: $Zn_8Se_2[BeGeO_4]_6$, bulk ZnSe and bulk ZnS; (bottom) (d) $Cd_8Te_2[BeGeO_4]_6$; (e) $Cd_8Se_2[BeGeO_4]_6$; (f) $Cd_8S_2[BeGeO_4]_6$; (g) coincident: bulk CdSe and bulk CdTe. Asterisks denote lamp artifacts.

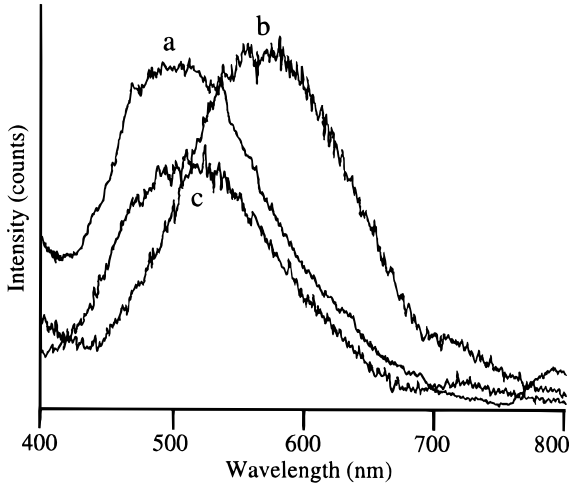

Figure 14. Room-temperature emission spectra of (a) $Cd_8Te_2[BeSiO_4]_6$, (b) $Cd_8Te_2[BeGeO_4]_6$, and (c) $(Cd_{0.7}Zn_{0.3})_8Te_2[BeGeO_4]_6$. The excitation wavelength is set at the maximum of each corresponding excitation spectrum and intensities are normalized.

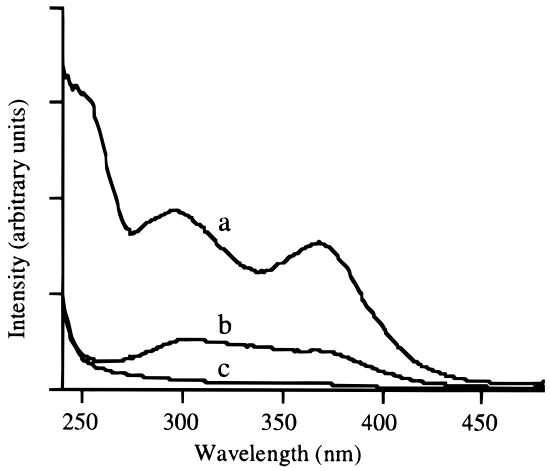

Figure 15. Corrected room-temperature photoexcitation (λ_{em} = 750 nm) spectra of single-crystal $Zn_8S_2[BeSi_xGe_{1-x}O_4]_6$, where (a) $x = 0.04$, (b) $x = 0.37$, and (c), $x = 0.74$.

precise stoichiometry of the intracage species directly affects the electronic relaxation mechanism in some manner. These results suggest that the emission energy and relative luminescence quantum yield are a function of *both* the intracage cation and anion; the helvite analogues behave as discrete $[M_4X]^{6+}$ moieties included within the sodalite framework host.

Photoluminescence Spectroscopy of the Single Crystals. The single crystals prepared in this study afford the opportunity to measure the photoluminescence properties of the helvite phases in the absence of any impurities, such as the bulk semiconductor. The room-temperature photoexcitation spectra of the $Zn_8S_2[BeSi_xGe_{1-x}O_4]_6$ single crystals, measured at an emission wavelength of 750 nm, are shown in Figure 15. The germanium-rich crystal exhibits three excitation maxima that give rise to the low-energy emission: one at or below 240 nm (the low-wavelength limit of the spectra) and two broad, lower intensity maxima centered at 295 and 368 nm. As the framework silicon content is increased, the high energy excitation maxima appear to blue-shift to wavelengths shorter than the instrument limit, analogous to the UV/vis absorption spectra (Figure 9).

The room-temperature emission spectra of the single crystals, powder solid solution end members and bulk ZnS are compared in Figure 16. The powder beryllogermanate emission is blue-shifted relative to that of bulk ZnS, but appears slightly red-shifted with respect to the emission maximum of the corresponding single crystal. Even with the small discrepancy in the measured emission energies, the photoemission spectra of the single crystals confirm that the visible energy emission (ca. 500 nm) observed in the germanium-rich helvite powders is intrinsic to the sodalite analogue and is not due to impurities or bulk semiconductor. The single-crystal spectra also show clearly that the sodalite analogues exhibit two emission bands; apparently after photoexcitation charge carriers are trapped in at least two distinct sites in the helvite structure, similar to the emission behavior observed with single-crystal $Zn_8O_2[BO_2]_{12}$.[17]

Conclusion

The composition-dependent optical and electronic tunability of the sodalite analogues with stoichiometries

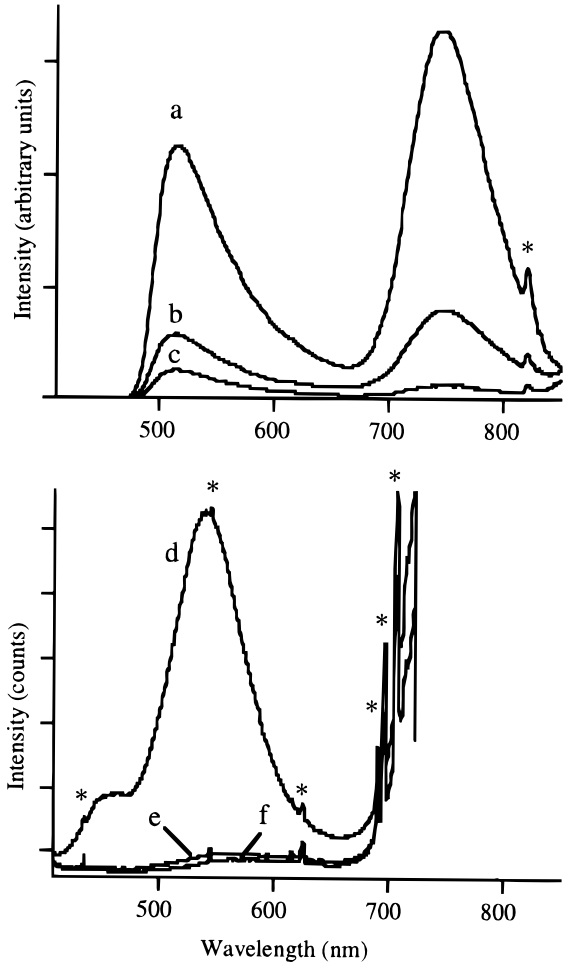

Figure 16. Room-temperature emission spectra of $Zn_8S_2[BeSi_xGe_{1-x}O_4]_6$ single crystals (top) (a) $x = 0.04$, (b) $x = 0.37$, (c) $x = 0.74$ ($\lambda_{ex} = 350$ nm), and powders (bottom) (d) $x = 0$, (e) $x = 1$, and (f) bulk ZnS ($\lambda_{ex} = 365 \pm 50$ nm) of equal sample volumes. Asterisks denote lamp artifacts.

$Zn_8X_2[BO_2]_{12}$ (X = O, S, Se) and $[Cd_yZn_{1-y}]_8X_2[BeSi_xGe_{1-x}O_4]_6$ (X = S, Se, and Te) has been demonstrated. The materials can be prepared either hydrothermally or by high-temperature solid-state reaction. The borate sodalite analogues crystallize with $I\bar{4}3m$ symmetry and the powder helvite analogues, in which the T1 and T2 framework cations are perfectly ordered, crystallize with $P\bar{4}3n$ symmetry and form solid solutions, over a range of framework compositions, that obey Vegard's law. Single crystals with stoichiometry $Zn_8S_2[BeSi_xGe_{1-x}O_4]_6$ ($x = 0.03$, 0.37, 0.74) exhibit additional weak X-ray diffraction peaks, not observed in the corresponding powder analogues, that are forbidden in $P\bar{4}3n$ symmetry. Assignment of $P23$ symmetry to these solid solutions is supported by selected area diffraction of the single crystals, and the lower symmetry apparently results from doping of the larger Ge atoms on Si sites.

The results presented show that as the relative amount of silicon in the framework increases, the unit-cell size decreases and the $[M_4X]^{6+}$ tetrahedra are contracted within the cage. As the size of the intracage atoms is increased, the rigid sodalite framework does not fully accommodate the expanded tetrahedra, and the intracage cations are forced closer to adjoining cages. Nevertheless, the anion−anion separations in these materials exceeds 6 Å, an appreciable distance that serves to isolate electronically the species within each cage. This isolation results in strong electronic localization as measured by the dramatic low-frequency shifts in the MAS NMR spectra of the cage center anions and the high energy shifts of the UV/vis absorption bands of these materials, relative to the bulk semiconductors. The smaller cage size of the beryllosilicates, and hence the smaller interatomic distances throughout the structure, serve to isolate the intracage species even more efficiently than is observed in the beryllogermanates.

After excitation by UV energy, the materials luminesce at room temperature and the beryllogermanates exhibit the most intense emission. The emission spectra consist of a broad, high-energy band strongly Stokes-shifted to the visible region and a lower energy band that extends to the near infrared region. At 77 K the excitation energy can be stored for several minutes, after which the visible emission is initiated by gentle heating of the sample. Photoluminescence spectroscopy of the single crystals shows that the emission bands in the visible region and at lower energy are intrinsic to the sodalite analogue. Additionally, in the beryllogermanates the luminescence maxima and relative quantum yield appear to vary as a function of the precise $[M_4X]^{6+}$ composition. Fine-tuning of the optical absorption and emission energies is possible by subtly modifying the host framework composition.

Acknowledgment. We thank Dr. Joe Hriljac of Brookhaven National Laboratory for collection of powder synchrotron data, Ines Winter of the University of Bonn and Stefanie Assmann of the University of Konstanz for assistance during the XANES measurements, and Dr. Vojislav I. Srdanov (UCSB) for many helpful discussions. K.L.M. gratefully acknowledges Professor Henry Offen (UCSB) for providing dedicated laboratory space for handling of the beryllium-containing materials. I.K. acknowledges a grant by Schweizerischer Nationalfonds. Funding for this project was provided by the NSF Science and Technology Center for Quantized Electronic Structures, Grant No. DMR 91-20007; by National Science Foundation Grant No. DMR89-13738 (HE); and by the Office of Navel Research (GDS).

Supporting Information Available: Final atomic coordinates, *R* factors, complete lists of bond distances and angles, and Figures 1−11 showing the final observed, calculated, and difference profiles for the Rietveld refinements of the powder helvite analogues; final atomic coordinates, anisotropic thermal parameters, and observed and calculated structure factors of the single crystals (34 pages). Ordering information is given on any current masthead page.

CM960168C